

Microburst Scale Size Distribution Derived with AeroCube-6

M. Shumko¹, T.P. O’Brien², J. Sample¹, A. Johnson¹, D.L. Turner², J.B.
Blake², B.A. Griffith¹, O. Agapitov³, S. Claudepierre²

¹Department of Physics, Montana State University, Bozeman, Montana, USA

²Space Science Applications Laboratory, The Aerospace Corporation, El Segundo, California, USA

³Space Sciences Laboratory, University of California Berkeley, Berkeley, California, USA

Key Points:

- The microburst size distribution in low Earth orbit and the magnetic equator was estimated.
- In low Earth orbit the majority of microbursts have a scale size on the order of a few tens of km.
- At the magnetic equator the size of most microbursts correspond to the scale of **highly** correlated and **high amplitude?** whistler-mode chorus waves.

Corresponding author: M. Shumko, msshumko@gmail.com

Abstract

Microbursts are an impulsive increase of electrons from the radiation belts into the atmosphere and has been directly observed in low Earth orbit and upper atmosphere. Microbursts are believed to be generated by wave-particle scattering between whistler mode waves and radiation belt electrons. Prior work has estimated that microbursts are capable of rapidly depleting the radiation belt electrons on the order of a day, hence their role to radiation belt electron losses must be considered. Radiation belt electron losses due to microbursts is not well understood, and more work is necessary to accurately quantify their contribution. To further address this question we present a statistical study of microburst scale sizes using the pair of AeroCube-6 CubeSats. The microburst scale size distribution in low Earth orbit and the magnetic equator was derived. In low Earth orbit, the majority of microbursts were found to have a size of less than a few tens of km with a minority of microbursts observed at a separation above 50 km. When mapped to the magnetic equator, the microburst scale size distribution corresponds to highly correlated and high amplitude ($> X$ pT) whistler mode chorus scale size derived in prior literature.

1 Plain Language Summary

<https://sharingscience.agu.org/creating-plain-language-summary/>

2 Introduction

Since the discovery of the Van Allen radiation belts in the 1960s by Van Allen (1959) and Vernov and Chudakov (1960), decades of research has made headway in understanding the dynamics particle acceleration and loss mechanisms. One of acceleration and loss mechanisms extensively studied is wave-particle scattering between whistler-mode chorus waves and electrons (Abel & Thorne, 1998; Meredith et al., 2002; Horne & Thorne, 2003; Thorne et al., 2005; Millan & Thorne, 2007; Bortnik et al., 2008). Whistler-mode chorus waves are typically generated by a temperature anisotropy of low energy electrons up to tens of kiloelectronvolts (keV) and are typically found in the $\sim 6-12$ magnetic local times (MLT) (Li, Thorne, Angelopoulos, Bortnik, et al., 2009; Li, Thorne, Angelopoulos, Bonnell, et al., 2009). Whistler-mode chorus waves interact with radiation belt electrons, and are widely believed to cause electron precipitation termed microbursts (Millan & Thorne, 2007).

Microbursts are a subsecond impulse of electrons that are observed by high altitude balloons and satellites in low Earth orbit (LEO) on the radiation belt magnetic footprints, $\sim 4-8$ L-shell (L) (Anderson & Milton, 1964; Parks, 1967; Lorentzen, Blake, et al., 2001; Lorentzen, Looper, & Blake, 2001; O'Brien et al., 2003; Woodger et al., 2015; Crew et al., 2016; Breneman et al., 2017; Mozer et al., 2018; Greeley et al., 2019). Microbursts' role as a radiation belt electron loss mechanism has been estimated to be significant, with total radiation belt electron depletion due to microbursts estimated to be on the order of a day (Lorentzen, Looper, & Blake, 2001; O'Brien et al., 2004; Thorne et al., 2005; Breneman et al., 2017).

One of the unconstrained microburst parameters that is critical to better quantify the role of microbursts as a loss mechanism is their physical size. Historically there have been various case studies that estimated microburst size. Parks (1967) found that the size of mostly low energy microbursts to be 40 ± 14 km. J. Blake et al. (1996) found a microburst with a size of a few tens of km using the the Solar Anomalous and Magnetospheric Particle Explorer (SAMPEX) and concluded that typically microbursts are less than a few tens of electron gyroradii in size (order of a few km in LEO). Dietrich et al. (2010) also used SAMPEX in another case study and concluded that the observed microbursts were smaller than 4 km. More recently, Crew et al. (2016) used the Focused

Investigation of Relativistic Electron Bursts: Intensity, Range, and Dynamics (FIREBIRD-II) CubeSats and found an example of a microburst larger than 11 km, and Shumko et al. (2018) used FIREBIRD-II to identify a microburst with a size greater than 51 ± 1 km. The large variance in prior results imply that there is a distribution of microburst scale sizes that this study aims to estimate.

Besides addressing the microburst role in radiation belt electron losses, the microburst size distribution is pertinent to identify the wave mode(s) responsible for scattering microbursts. The microburst size distribution in LEO can be mapped to the magnetic equator and the mapped microburst size distribution compared to various wave scales derived in prior literature to identify the dominant wave properties responsible for scattering microburst electrons.

This study addresses these two questions by estimating the microburst size distribution in LEO and the magnetic equator. The twin AeroCube-6 (AC6) CubeSats are utilized for this study because they are ideally equipped for observing microbursts and they took data simultaneously over a span of three years while their separation varied between 2 and 800 km. This paper first describes the AC-6 mission, including their orbit and instrumentation. Then the procedure undertaken to identify microbursts observed by each spacecraft and how they are combined to make a list of the temporally coincident microbursts is described. Next, the microburst size distributions in LEO and the magnetic equator as a function of spacecraft separation is derived. Then a model is developed to understand how various microburst size distributions will be seen by a two-point measurement. Lastly, we discuss and summarize these results and infer the properties of the whistler-mode chorus waves that are believed to cause microbursts.

3 Instrumentation

The AC6 mission consists of a pair of 0.5U (10x10x5 cm) CubeSats built by the Aerospace Corporation and launched on June 19th, 2014 into a 620 x 700 km, 98 degree inclination orbit. The two satellites, designated as AC6-A and AC6-B separated after launch and drifted apart. AC6 has an active attitude control system which allows them to change their differential drag to allow fine separation control. Figure 1a shows the AC6 separation for the duration of the mission.

Each AC6 unit is equipped with a three Aerospace microdosimeters (licensed to Teledyne Microelectronics, Inc). The dosimeter used for this study is dos1 and is identical on both AC6 units. Dos1 has a 30 keV electron threshold and samples at 10 Hz. The AC6 orbit is in the dawn-dusk MLT sectors and Fig. 1b shows the number of quality 10 Hz samples taken simultaneously by AC6 as a function of L and MLT. Quality samples have a 0 data quality flag. The quality flag and detailed technical information on AC6 is described in O'Brien et al. (2016).

4 Methodology

4.1 Microburst Detection

The first step to find microbursts observed simultaneously by both spacecraft is to identify them from each spacecraft separately. We have detected microbursts with two different methods that yielded quantitatively similar results. The first method is the burst parameter (O'Brien et al., 2003). This algorithm has been successfully used in other microburst studies, mainly with the microbursts observed by the Solar Anomalous and Magnetospheric Particle Explorer add citations. For AC6, we found that a burst parameter threshold of 5 has good trade-off between false positive and false negative microburst detections. Another microburst detection algorithm based on wavelet spectra frequency

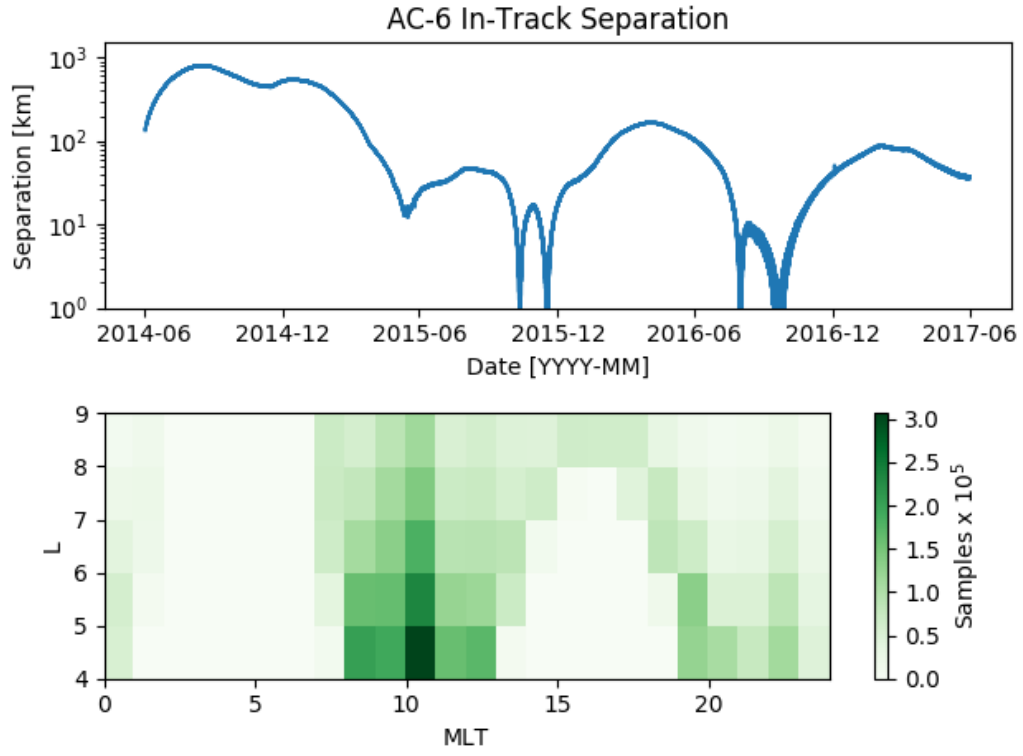


Figure 1. AC6 mission distributions for (a) spacecraft separation and (b) number of simultaneous 10 Hz samples as a function of L and MLT.

filtering was developed and the resulting list of microbursts is similar to the list from the burst parameter. **Talk about the wavelet based detector as well?**

The transmitters on AC6 can cause unphysical count impulses in the dosimeters that resembles periodic trains of microbursts. These false detections were removed to remove their bias. One source of transmitter noise was observed at times when AC6 was in contact with the ground stations above mainland US for data downloads and commanding thus the mostly low L detections made above the US were discarded.

Another source of noise is crosslink transmissions between the AC6 units. These transmissions occurred when either spacecraft transitioned from the survey mode to 10 Hz mode. This noise is sometimes not caught by the data quality flag, so the following empirically-derived criteria was developed to remove those detections. The dosimeter with a 250 keV nominal electron threshold, dos2 was used because it had a similar response to noise while rarely responded to microbursts. Since the transmitter noise is very periodic, cross-correlation (CC) and autocorrelation (AC) methods were applied to the dos1 and dos2 time series. Detections were removed if the following two criteria were met: either dos1 or dos2 time series had a AC peak at a 0.2 or 0.4 s lag, and the dos1-dos2 CC was greater than 0.9. The AC lag criteria alone sometimes falsely removed legitimate trains of microbursts, so the second criteria insured that the detection was removed if there was a very high correlation across an order of magnitude in energy.

The lists of microbursts observed by either AC6 unit were merged into a temporally coincident list with the following procedure. **Show the microburst detection cartoon I've showed in conferences?** The general idea is that a microburst detection on one spacecraft will CC well with the time series from the other spacecraft if it observed a similar microburst, and poorly if there was no microburst observed by the other spacecraft. Each microburst detection made by either spacecraft was CC with the time series from the other spacecraft. Windows of 1 and 1.2 s were used to CC the time series. Different window sizes were used to account for numerical uncertainty due to Poisson noise. Microbursts detections with a CC above 0.8 were considered temporally coincident. This CC threshold was chosen as it is low enough to identify temporally coincident microbursts superposed with noise, and high enough to reject most non-coincident events. Figure 2, panels (a), (c), and (e) show examples of microbursts observed by both AC6 units when they were separated by 6, 17, and 69 km, respectively.

The last CC criteria required that the temporal CC must be greater than the spatial CC + 0.3. The spatial CC was calculated by shifting the AC6-B time series by the in-track lag to CC in latitude. This criteria was applied to remove curtains, spatially stationary and narrow in latitude structures observed by AC6 (J. B. Blake & O'Brien, 2016) and sometimes appear as microbursts. Figure 2, panels (b), (d), and (f) show the AC6 spatially aligned time series to confirm that the three cases shown were indeed microbursts. The coincident microburst list was then spot checked by two authors to any remove poorly correlated events. Considering the CC criteria and data availability, 662 confirmed simultaneous microburst detections are used to calculate the microburst size distribution in the following section.

4.2 Microburst Size Distribution in LEO and Magnetic Equator

The list of temporally coincident microbursts, which from now on will just be called microbursts, is now compiled to show the fraction of microbursts observed above a separation s . When AC6 observes a microburst at s , the microburst's size must be greater than s . This fact, along with the arguments presented in Section 4 in Joy et al. (2002), is used to investigate the dependence of the number of microbursts observed above s , as a function of s which is the microburst complementary cumulative distribution $F(s)$.

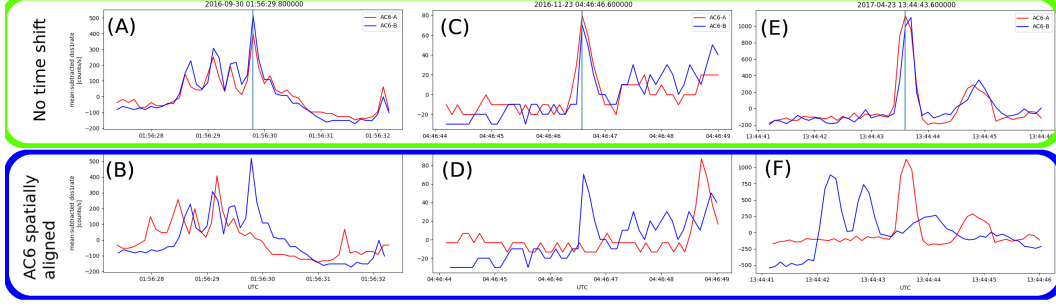


Figure 2. Examples of microbursts observed simultaneously by AC6. Panels (a), (c) and (e) shows the temporally-aligned time series at spacecraft separations of 5.6 km, 16.5 km, and 68.5 km, respectively. Panels (b), (d), and (f) show the spatially aligned time series corresponding to the time series in the same column. The clear temporal correlation and lack of spatial correlation demonstrates that these events are microbursts.

Include the following Bayes theorem proof? It does not seem necessary (or I did not motivate it) If $P(A)$ is the probability that a microburst is larger than s and $P(B)$ is the probability that AC6 is separated by s , then the fraction of microbursts observed at s is the conditional probability $P(A | B)$. Using Bayes theorem,

$$P(A | B) = \frac{P(A \& B)}{P(B)} \quad (1)$$

where $P(A \& B)$ is the joint probability. Since the AC6 separation is independent of microburst size, $P(A \& B) = P(A)P(B)$. Hence

$$P(A | B) = \frac{P(A)P(B)}{P(B)} = P(A) \quad (2)$$

so AC6 is observing the probability that the microburst is larger than s .

The cumulative number of microbursts observed above s is the ratio of $N(s)$, the number of microbursts observed above s to $N(0)$, the total number of microbursts observed

$$F(s) = \frac{N(s)}{N(0)} \quad (3)$$

$$N(s) = \sum_{i=s}^{\infty} n_i \frac{S_{max}}{S_i} \quad (4)$$

where n_i is the number of microbursts observed by AC6 in i th bin. The normalization term S_{max}/S_i is a ratio of the number of samples observed in the most sampled bin to the number of samples in i th bin. This normalization factor corrects for AC6's non-uniform sampling in separation and the number of samples is shown in Fig. 3c. With this normalization, $F(s)$ can be interpreted as the fraction of microbursts observed above s assuming AC6 sampled evenly in separation. Microburst $F(s)$ in LEO is shown by the black curve in Fig. 3a for $4 < L < 8$ and split into one L -wide bins with the colored curves. The separation bin width used in Fig. 3 is 5 km. To check for bias in $F(s)$ due to the separation bins, $F(s)$ was resampled with other bin widths and offsets. Bin widths as large as the size of the features in $F(s)$ (20–30 km) and bin offsets up to 50% of the bin width did not qualitatively effect the curves in Fig. 3a.

The overall trend in Fig. 3a consists of a sudden cumulative probability drop off, followed by a shoulder up to $s \approx 70$ km where the cumulative distribution drops to nearly

zero. The shaded region around the black curve shows the standard error due to counting statistics. The uncertainty due to false coincidence events i.e. two unrelated microbursts randomly lining up in time was also considered. The microburst duty cycle in a one minute window ($\approx 1 L$) around each microburst was calculated. The false coincidence probability is the square of the duty cycle and was found to be less than 5% for the majority of microbursts. The false coincidence probability for each microburst was then used to randomly remove microbursts and $F(s)$ was recalculated in 1000 trials. The uncertainty in $F(s)$ with microbursts randomly removed was much smaller than the uncertainty due to counting statistics alone. Lastly, Fig. 3b shows the microburst probability density (PD), calculated by differentiating $F(s)$, and shows a peak at $s < 20$ km as well as a peak between 70-80 km separation.

To compare the microburst size to the size of their progenitor waves, the spacecraft locations during observed microbursts were mapped to the magnetic equator using the Olson-Pfitzer magnetic field model (Olson & Pfitzer, 1982) which is implemented with a Python wrapper for IRBEM-Lib (Boscher et al., 2012). As previously stated, a microburst observed in LEO has a size larger than the spacecraft separation, hence that microburst would also have a size larger than the spacecraft separation after it was mapped to the magnetic equator. Thus the procedure to estimate $F(s)$ is identical to the LEO size distribution but with a different normalization. The normalization factors were calculated by mapping every quality AC6 sample taken simultaneously to the magnetic equator and binning them by equatorial separation into 100 km bins. Figure 4 shows the equatorial microburst size distribution in the same format as Fig. 3. Similar to the microburst PD in LEO, most of the equatorial microburst PD was observed when the AC6 equatorial separation was less than 300 km.

The results in Figs. 3 and 4 show the fraction of microbursts observed above a spacecraft separation and do not fully represent the microbursts size distribution due to the compounding effects from the range of microburst sizes and random locations of microbursts with respect to AC6 i.e. even if the microburst size is much larger than s , a fraction of those microbursts will graze only one AC6 unit and not be observed by the other. Thus modeling is necessary to capture the compounding influence of these statistical effects on AC6, a two-point measurement.

5 Modeling the Distribution of Microburst Sizes

5.1 Monte Carlo and Analytic Models to Estimate $F(s)$

To account for the effects due to microbursts randomly occurring in the vicinity of AC6 with an unknown distribution of microburst sizes, Monte Carlo (MC) and analytic models were developed. These models assume a hypothesized distribution of microburst sizes expressed with a probability density function $P(r)$, and a microburst geometry to estimate $F(s)$. Microbursts are assumed to be circular with a radius r . A few distribution of microburst size hypotheses are considered: a one-size microburst population, a two-size microburst population, and \times continuous $P(r)$.

The MC model is the most intuitive to understand and it consists of randomly scattering 10^5 microburst centers in a 400 x 400 km grid around AC6 of various r that are distributed according to $P(r)$. Spacecraft A is placed at the origin, and spacecraft B is placed along the positive y-axis at predetermined distances from the origin corresponding to the AC6 separation bins used in Section 4.2. Then the cumulative number of simultaneously observed microbursts at spacecraft A and each spacecraft B location was counted.

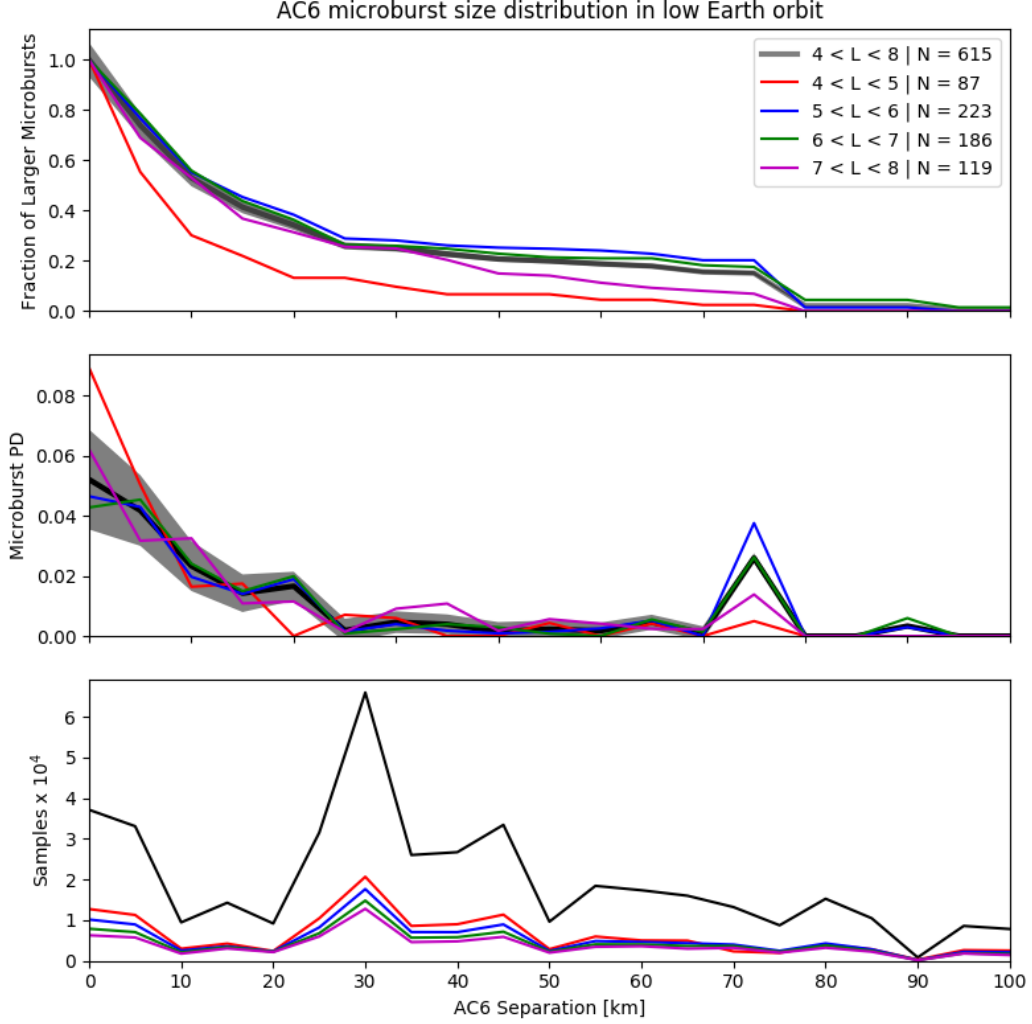


Figure 3. Fraction of microbursts greater than the spacecraft separation as a function of separation in LEO. Panel (a) shows the fraction of microbursts observed above that separation. Panel (b) shows the microburst probability density as a function of separation. Lastly, panel (c) shows the number of simultaneous samples AC6 observed as a function of separation. The colored lines show the distributions binned by L , and the thick black curve shows the fraction of microbursts observed above a separation in the entire radiation belt ($4 < L < 8$). The gray shading around the black curve shows the uncertainty due to counting statistics.

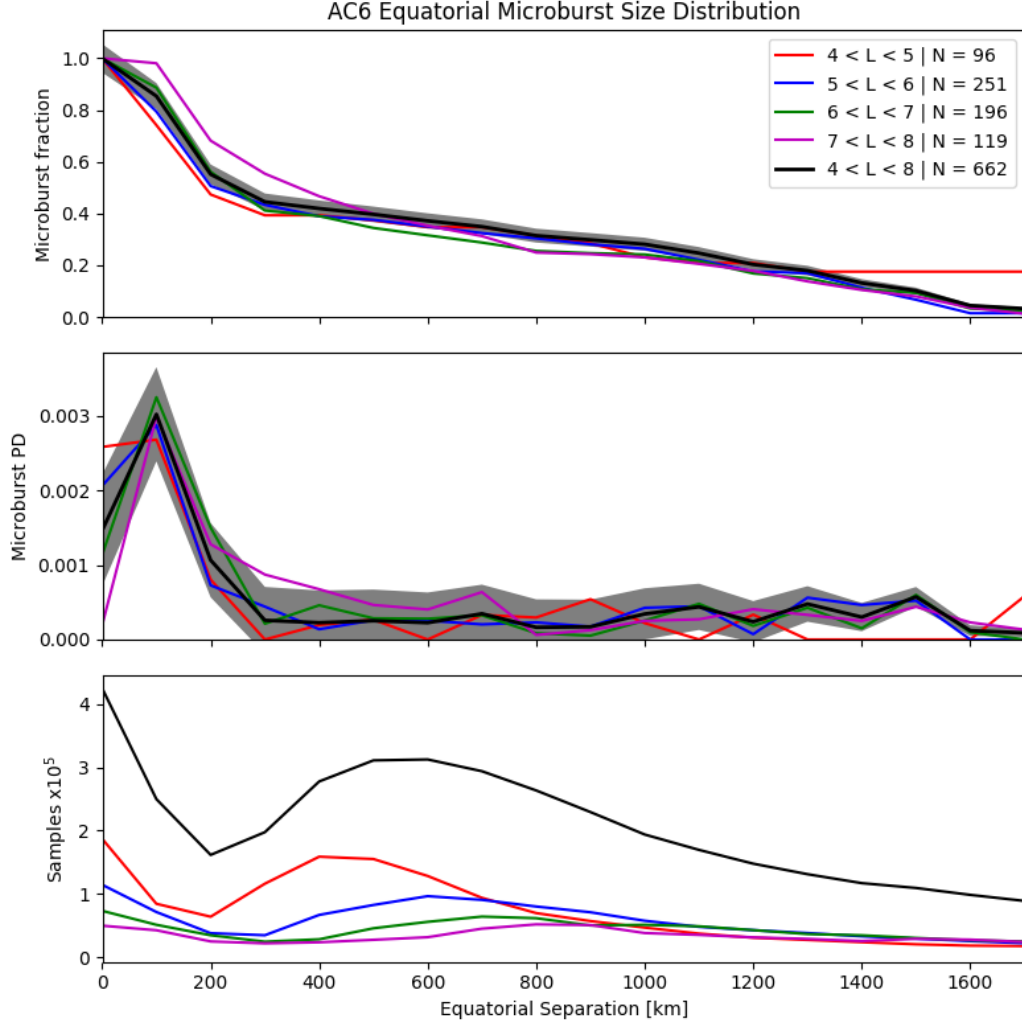


Figure 4. Microburst scale size distribution in the same format as Fig. 3 and mapped to the magnetic equator.

The modeled fraction of microbursts observed above s is then

$$F(s) = \frac{\sum_{i>s}^{\infty} n_i}{\sum_{i>0}^{\infty} n_i}. \quad (5)$$

where as before the number of microbursts observed by both spacecraft in i th bin is n_i .

The analytic model, while identical to the MC model, highlights the geometrical concepts connecting the microburst size distribution and $F(s)$. Assuming that microbursts are circular with radius r and AC6 are separated by s , there is an area where a microburst will be observed by both spacecraft. Figure 5a shows this geometry with the two spacecraft indicated with the black dots. All microbursts whose center lies inside the circular area of radius r that surrounds the top spacecraft will be observed by the top spacecraft. Likewise the same argument applies to the bottom spacecraft. The intersection of these two areas defines another area, $A(r, s)$ where a microburst will be observed by both spacecraft and is given by the circle-circle intersection area equation,

$$A(r, d) = 2r^2 \cos^{-1} \left(\frac{d}{2r} \right) - \frac{d}{2} \sqrt{4r^2 - d^2}. \quad (6)$$

Cite anything? Wolfram: <http://mathworld.wolfram.com/Circle-CircleIntersection.html>
Example geometries with an overlapping area are shown in Fig. 5b and c.

The circle intersection area can be thought of as a probability that a microburst will be observed by both spacecraft, given that it was observed by one. The hypothesized $P(r)$ can be thought of as the relative occurrence of microbursts at various r and is effectively a weighting factor on $A(r, s)$ which is integrated out (marginalized) since AC6 is observing the overall effect of microbursts at all r . Lastly, a cumulative integral over a dummy variable s' is applied to the normalized areas to calculate $F(s)$. With these considerations the analytic $F(s)$ is given by

$$F(s) = \frac{\int_0^{\infty} \int_0^{\infty} A(r, s') P(r) dr ds'}{\int_0^{\infty} \int_0^{\infty} A(r, s') P(r) dr ds'}. \quad (7)$$

where as in the MC model the denominator is the normalization factor. To illustrate the effects of random microburst locations around AC6, example analytic and MC model $F(s)$ assuming a fixed-size 40 km diameter microburst population is shown in Fig. 5d with the dashed blue and red curves, respectively.

5.2 Estimating optimal parameters for microburst size models

At this stage a few hypothesized microburst size distributions are tested and optimal model parameters estimated. For each hypothesized microburst size distribution, Bayesian inference is used to estimate the optimal model parameters with a Metropolis Markov Chain Monte Carlo (MCMC) sampler (Metropolis et al., 1953). Bayes theorem is central to Bayesian inference. For an observed $F(s)$ denoted here by x , and model parameters θ Bayes theorem can be written as

$$P(\theta|x) = \frac{P(x|\theta)P(\theta)}{P(x)} \quad (8)$$

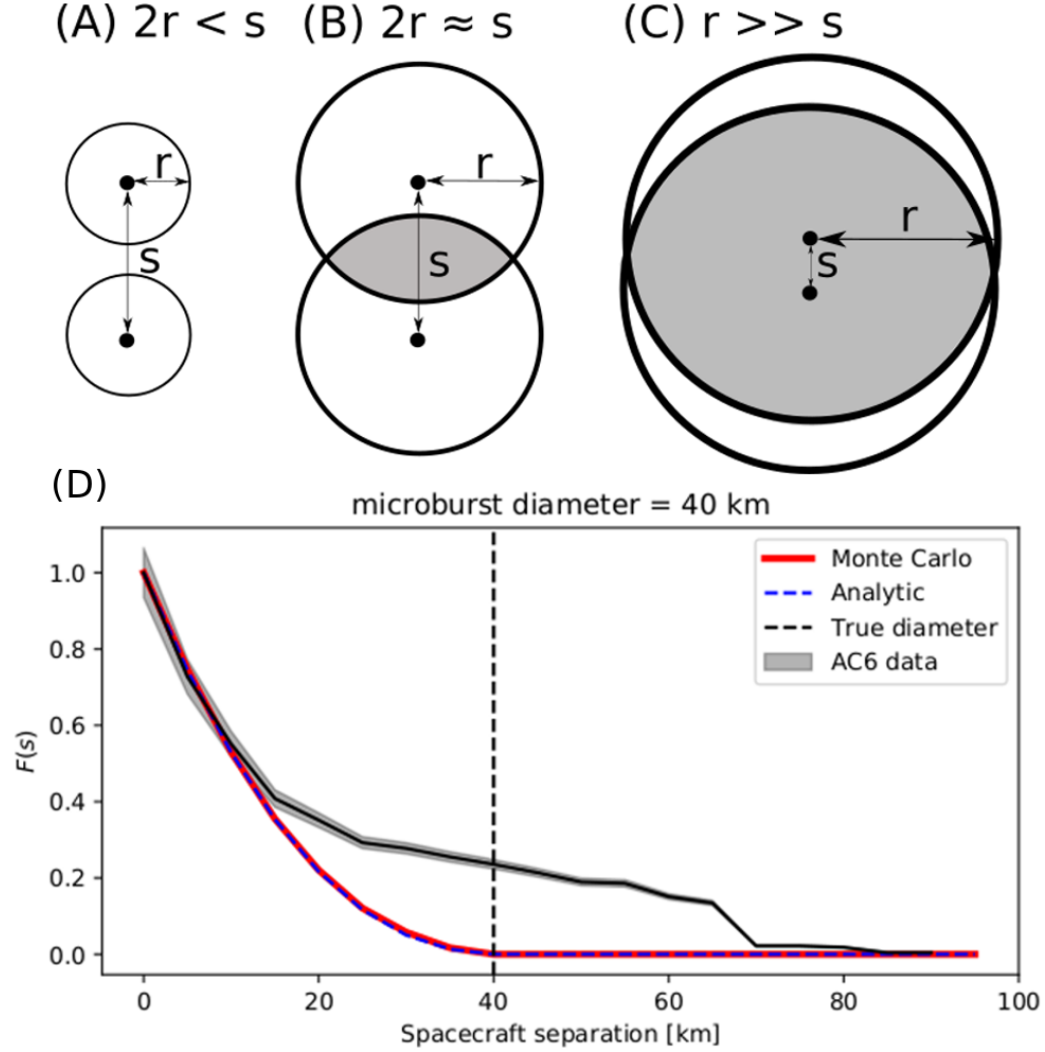


Figure 5. Panels A-C show the geometry of the analytic model. The two spacecraft are shown as black dots. The enclosing black circle around each spacecraft bounds the area where a microburst will be observed by one or both AC6 units if the microburst's center lies inside the circle. Panel (A) shows the case where microburst diameter is smaller than the AC6 separation and all microbursts will be observed by either unit A or B and never simultaneously. Panel (B) shows the intermediate case where the microburst diameter is comparable to the AC6 separation and some fraction of microbursts will be observed simultaneously. The fraction of the microbursts simultaneously observed is proportional to the circle intersection area shown with grey shading. Panel (C) shows the case where the spacecraft separation is much smaller than the microburst size and nearly all microbursts will be observed by both spacecraft. Lastly panel (D) shows $F(s)$ from the AC6 data with a solid black line, and a MC and analytic $F(s)$ for a single-sized microburst distribution with a 40 km diameter.

where $P(\theta)$ is the prior that is a PDF that describes the level of knowledge, however weak, about the model parameters. The likelihood is $P(x|\theta)$ and it describes the probability of obtaining the observations given model parameters. In this analysis the MC microburst model is used in the likelihood to model $F(s)$ and estimate the probability that the modeled $F(s)$ represents x . The posterior is $P(\theta|x)$ that is the model parameter probability distributions given the data. The posterior is used here to make conclusions regarding the model parameters after assuming a likelihood function and prior knowledge of the model parameters. Lastly, $P(x)$ is the marginal likelihood that describes the probability of obtaining x after marginalizing over all prior variables. Calculation of $P(x)$ is difficult, and often not necessary for model parameter estimation.

With all of the above terminology, the important takeaway is that the posterior distribution for each model parameter is interpreted as the range of θ consistent with x . A 95% credible interval (CI) is reported here that is interpreted as: assuming the hypothesized microburst size distribution, there is a 95% probability that the true model parameter is inside the CI. The Metropolis sampler is used to sample the posterior distribution.

While the Metropolis sampler is explained in detail in Metropolis et al. (1953) and a good introduction given in Sambridge et al. (2006), a brief overview is warranted. The Metropolis sampler samples the posterior distribution in N trials and for each trial a random set of model parameters is chosen from the prior. After the first set of model parameters, the Metropolis MCMC chooses a new set of parameters. If the prior probability of the new set of parameters multiplied by the likelihood is higher the current parameter set, the MCMC accepts the new parameter set, otherwise there is a probability that the new value will be accepted or rejected. The unique accept/reject property results with the sampler tending to more likely model parameters, while also exploring the neighboring regions. After the N trials a histogram is made from the accepted parameters to produce the posterior distribution.

The one-size microburst population model is explored first and the microburst PDF is given by

$$P(d) = \delta(s - d) \quad (9)$$

where δ is the Dirac Delta function and d is the diameter of all microbursts. The range of d that is consistent with the observed $F(s)$ is shown in Fig. 6. With this model, the microburst size is between 38 and 129 km with the optimal size of 73 km, estimated from the minimum least squares.

A generalization of the one-size model is a two-size microburst population model that assumes the following microburst PDF

$$P(d) = a\delta(s - d_0) + (1 - a)\delta(s - d_1) \quad (10)$$

where the diameters of the two microburst populations is given by d_0 and d_1 and a is the parameter encoding the relative fractions of the two populations. The result of this model is shown in Fig. 7. The fit is slightly better than the one-size model, although that is to be expected assuming the two more free model parameters. A majority, 98 % of microbursts have a size between 12 and 47 km with a rare population with a size between 76 and 234 km. The parameter set that minimizes the least squares penalty function is 99.5 % of microbursts are small with a size of 21 km and the 0.5 % of microbursts with a size of 140 km.

6 Discussion

The LEO microburst $F(s)$ estimated in section 4.2 shows that a majority of co-incident microburst were observed by AC6 when they were separated by less than a few

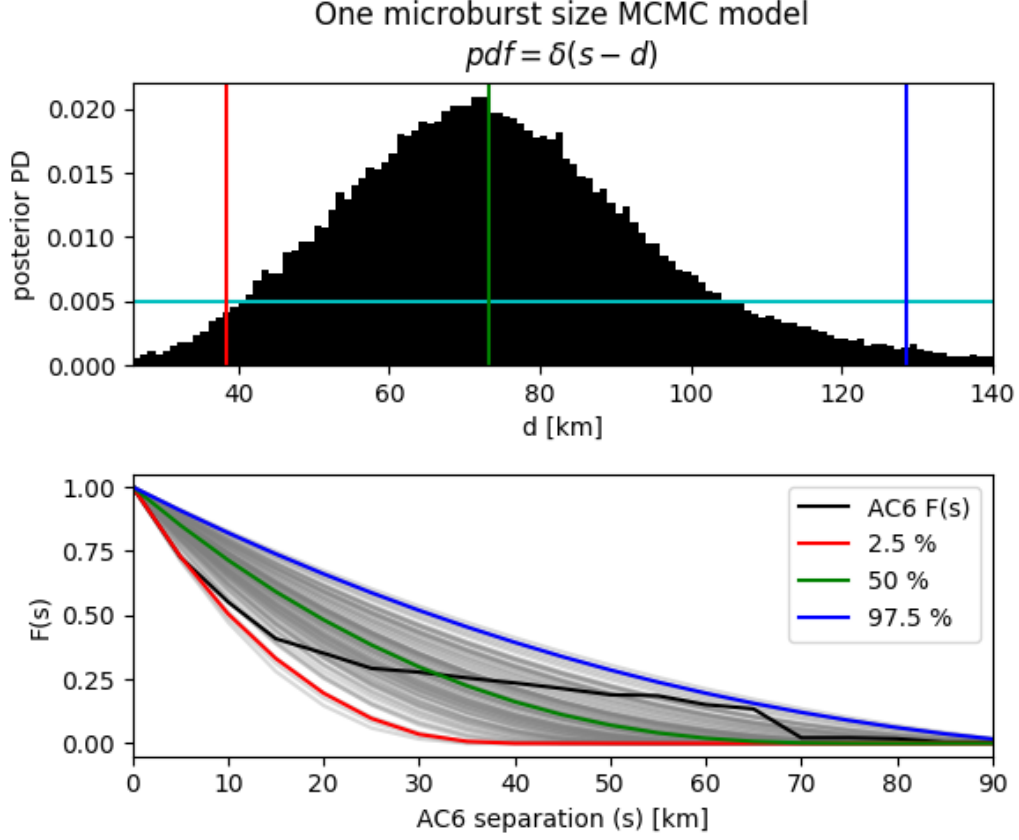


Figure 6. Range of plausible microburst sizes assuming all microbursts are one size. Panel a shows the posterior probability density (PD) of microburst diameters in black. The red, green, and blue vertical lines at 38, 73, and 129 km represent the 2.5, 50, and 97.5 posterior percentiles, respectively. A uniform prior between 0 and 200 km was assumed for this MCMC run. The prior PD is shown with the horizontal cyan line. Panel b shows the AC6 $F(s)$ for $4 < L < 8$ in black and 1000 $F(s)$ gray curves from microburst diameters randomly picked from the posterior. At each s , the 2.5, 50 and 97.5 $F(s)$ percentiles were estimated from the 1000 random $F(s)$ curves and are shown with the red, green, and blue curves, respectively.

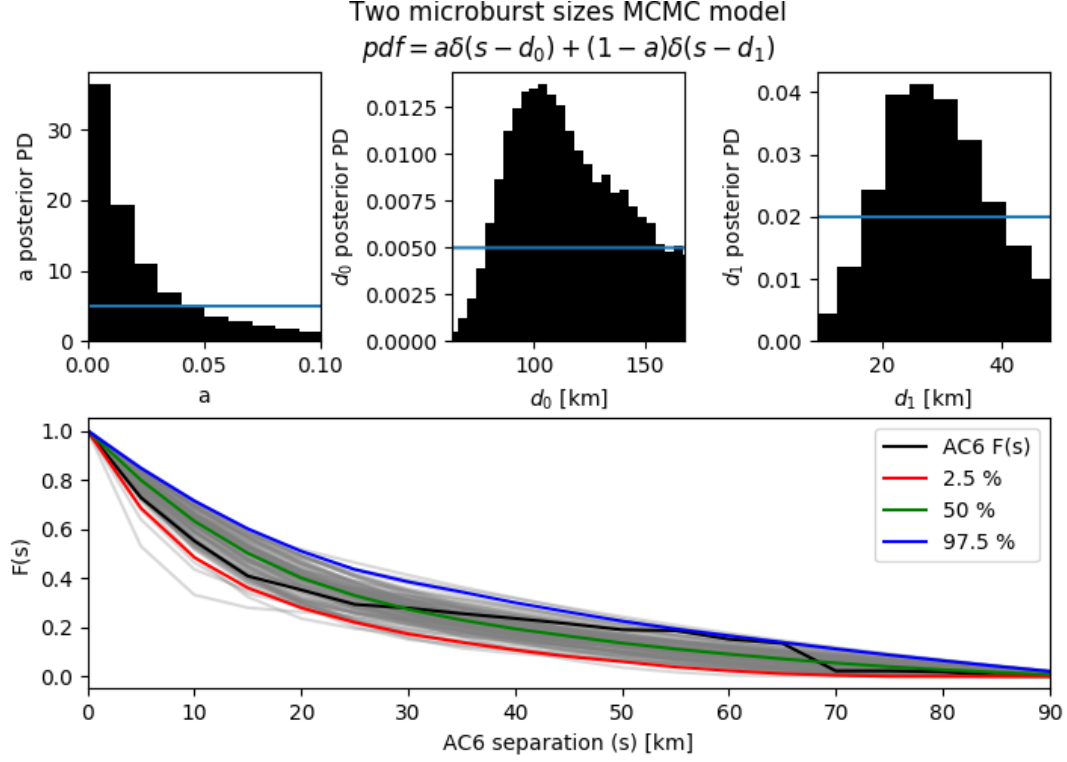


Figure 7. Range of plausible microburst sizes assuming the microburst population is composed of two sizes with a mixing term to describe their relative occurrence. Panel a shows the posterior distribution for the microburst population mixing term, a with a median value of 0.02. The a prior was uniform between 0 and 0.2. Panel b shows the posterior distribution for d_0 , the larger microburst population estimated with a uniform prior between 50 and 200 km and the posterior median diameter of 122 km. Panel c shows the posterior distribution for d_1 , the smaller microburst population estimated with a uniform prior between 0 and 50 km with a median diameter of 28 km. Panel d is similar to Fig. 6b and shows the AC6 $F(s)$ for $4 < L < 8$ in black, and randomly chosen $F(s)$ curves generated from 1000 sets of a , d_0 , and d_1 parameters from the posterior in grey. At each s , the 2.5, 50 and 97.5 $F(s)$ percentiles were estimated and shown with the red, green, and blue curves, respectively.

tens of km. When taken in context with prior literature, the LEO microburst size distribution calculated here is consistent with prior microburst size estimates. These results are most similar to citeAParks1967 who reported that > 15 keV microbursts are 40 ± 14 km and the bouncing packet example shown in J. Blake et al. (1996) with a size of “at least a few tens of kilometers”. The AC6 microburst size distribution is much larger than the sizes reported in Dietrich et al. (2010) who used very low (VLF) frequency transmission paths and SAMPEX and concluded that microbursts must be smaller than 4 km from a small number of microbursts observed during one SAMPEX pass. Furthermore, Dietrich et al. (2010) used the coincidence of microbursts and FAST events, subsecond VLF transmission perturbations, to make their conclusions while the connection between FAST events and microbursts is not well understood. Lastly, these results are consistent with FIREBIRD-II observations of a > 11 km microburst reported by Crew et al. (2016).

The microbursts observed by AC6 up to $s \approx 70$ km are consistent with the > 51 km bouncing packet microburst reported in Shumko et al. (2018). The microburst probability density shown in Fig. 3b shows that there is evidence of two microburst populations. The quality of the AC6 data is insufficient to definitively conclude that there are two distinct microburst populations. Assuming these two populations are real, the different microburst sizes may be distinguished by their energies as suggested by J. Blake et al. (1996) who noted that the > 150 keV and > 1 MeV microbursts are not always well correlated e.g. Fig. 10 in J. Blake et al. (1996).

The model results from section 5 emphasizes that care must be taken to interpret the $F(s)$ curves observed by AC6 and the true microburst size distribution due to the compounding effects of an unknown microburst size distribution, unknown microburst shape, and random microburst locations near AC6. The one-size model results in Fig. 6 show that there is a 95% probability that the microburst size is somewhere between 38 and 129 km, a relatively wide range of values. The two-size model shown in Fig. 7 does better at encompassing the AC6 $F(s)$, which is expected with the addition of two more free parameters. The two size model is interpreted as 98% of microbursts sizes are between 12 and 47 km and larger microbursts being very uncommon. A variety of continuous microburst size distributions such as the Maxwellian, Weibull and log-normal were also explored with similar results and are not shown. Due to lack of prior observations and theoretical predictions, it is difficult to identify an appropriate microburst size distribution hypothesis.

Show the optimal values.

The equatorial microburst $F(s)$ estimated in section 4.2 can be compared to prior multi-point measurements of chorus source sizes made near the magnetic equator. The International Sun-Earth Explorers (ISEE 1 and 2) were used by Gurnett et al. (1979) to make one of the first direct chorus source scale measurements. Gurnett et al. (1979) estimated that the wave power correlation scale was on the order of a few hundred kilometers across the background magnetic field. Using the Cluster Wide Band Data measurements Santolik et al. (2003) found the correlation scale of whistler mode chorus waves to be around 100 km near the source region at $L \approx 4$ and midnight MLT sector. Recently Agapitov et al. (2010, 2011, 2017, 2018) used a few sets of spacecraft with wave measurements near the chorus source region to statistically show that the extent of chorus source region can extend from 600 km in the outer radiation belt to greater than 1,000 km in the outer magnetosphere.

With the prior wave size estimates and microburst probability density from Fig. 4b in mind, it appears that the majority of microbursts have an equatorial size less than ≈ 200 km when compared to the two-point measurements made at high altitude inside the outer radiation belt. Assuming that chorus waves scatter electrons as in prior literature e.g. (Lorentzen, Blake, et al., 2001; Breneman et al., 2017), then the chorus waves that scatter microburst electrons on those scales must have particular wave properties

i.e. the wave properties critical to microburst scattering must be similar on scales corresponding to the equatorial microburst size. The wave properties necessary for scattering microburst electrons e.g. coherence, polarization, wave normal angle, can be identified by studying waves that are only observed for small spacecraft separations. These properties can then aid wave-particle scattering model development by constraining the wave properties and scattering modes responsible for scattering microburst electrons. Optimistically, these models may then be capable of predicting the distribution of microburst sizes that should be observed in LEO.

7 Conclusions

In conclusion, the twin AC6 CubeSats are

Talk about how these sizes fit in with prior work and how they can be used to estimate microburst loss rates.

To disentangle these compounding effects, a x-ray imager on board a high altitude balloon can determine the microburst size and shape without ambiguity from the distributions of x-rays created when microburst electrons scatter in the atmosphere.

Acknowledgments

This work was supported by NASA Headquarters under the NASA Earth and Space Science Fellowship Program - Grant 80NSSC18K1204. The AC6 data is available at <http://rbspgway.jhuapl.edu/ac6> and IRBEM-Lib version used for this analysis can be downloaded from <https://sourceforge.net/p/irbem/code/616/tree/>.

References

- Abel, B., & Thorne, R. M. (1998). Electron scattering loss in earth's inner magnetosphere: 1. dominant physical processes. *Journal of Geophysical Research: Space Physics*, 103(A2), 2385–2396.
- Agapitov, O., Blum, L. W., Mozer, F. S., Bonnell, J. W., & Wygant, J. (2017). Chorus whistler wave source scales as determined from multipoint van allen probe measurements. *Geophysical Research Letters*, n/a–n/a. Retrieved from <http://dx.doi.org/10.1002/2017GL072701> (2017GL072701) doi: 10.1002/2017GL072701
- Agapitov, O., Krasnoselskikh, V., Dudok de Wit, T., Khotyaintsev, Y., Pickett, J. S., Santolik, O., & Rolland, G. (2011). Multispacecraft observations of chorus emissions as a tool for the plasma density fluctuations' remote sensing. *Journal of Geophysical Research: Space Physics*, 116(A9), n/a–n/a. Retrieved from <http://dx.doi.org/10.1029/2011JA016540> (A09222) doi: 10.1029/2011JA016540
- Agapitov, O., Krasnoselskikh, V., Zaliznyak, Y., Angelopoulos, V., Le Contel, O., & Rolland, G. (2010). Chorus source region localization in the earth's outer magnetosphere using themis measurements. *Annales Geophysicae*, 28(6), 1377–1386. Retrieved from <http://www.ann-geophys.net/28/1377/2010/> doi: 10.5194/angeo-28-1377-2010
- Agapitov, O., Mourenas, D., Artemyev, A., Mozer, F., Bonnell, J., Angelopoulos, V., ... Krasnoselskikh, V. (2018). Spatial extent and temporal correlation of chorus and hiss: Statistical results from multipoint themis observations. *Journal of Geophysical Research: Space Physics*, 123(10), 8317–8330.
- Anderson, K. A., & Milton, D. W. (1964). Balloon observations of X rays in the auroral zone: 3. High time resolution studies. *Journal of Geophysical Research*, 69(21), 4457–4479. Retrieved from <http://dx.doi.org/10.1029/JZ069i021p04457> doi: 10.1029/JZ069i021p04457

- Blake, J., Looper, M., Baker, D., Nakamura, R., Klecker, B., & Hovestadt, D. (1996). New high temporal and spatial resolution measurements by sam-pex of the precipitation of relativistic electrons. *Advances in Space Research*, 18(8), 171 - 186. Retrieved from <http://www.sciencedirect.com/science/article/pii/0273117795009698> doi: [http://dx.doi.org/10.1016/0273-1177\(95\)00969-8](http://dx.doi.org/10.1016/0273-1177(95)00969-8)
- Blake, J. B., & O'Brien, T. P. (2016). Observations of small-scale latitudinal structure in energetic electron precipitation. *Journal of Geophysical Research: Space Physics*, 121(4), 3031–3035. Retrieved from <http://dx.doi.org/10.1002/2015JA021815> (2015JA021815) doi: 10.1002/2015JA021815
- Bortnik, J., Thorne, R., & Inan, U. S. (2008). Nonlinear interaction of energetic electrons with large amplitude chorus. *Geophysical Research Letters*, 35(21).
- Boscher, D., Bourdarie, S., O'Brien, P., Guild, T., & Shumko, M. (2012). *Irbem-lib library*.
- Breneman, A., Crew, A., Sample, J., Klumpar, D., Johnson, A., Agapitov, O., ... others (2017). Observations directly linking relativistic electron microbursts to whistler mode chorus: Van allen probes and FIREBIRD II. *Geophysical Research Letters*.
- Crew, A. B., Spence, H. E., Blake, J. B., Klumpar, D. M., Larsen, B. A., O'Brien, T. P., ... Widholm, M. (2016). First multipoint in situ observations of electron microbursts: Initial results from the NSF FIREBIRD II mission. *Journal of Geophysical Research: Space Physics*, 121(6), 5272–5283. Retrieved from <http://dx.doi.org/10.1002/2016JA022485> (2016JA022485) doi: 10.1002/2016JA022485
- Dietrich, S., Rodger, C. J., Clilverd, M. A., Bortnik, J., & Raita, T. (2010). Relativistic microburst storm characteristics: Combined satellite and ground-based observations. *Journal of Geophysical Research: Space Physics*, 115(A12).
- Greeley, A., Kanekal, S., Baker, D., Klecker, B., & Schiller, Q. (2019). Quantifying the contribution of microbursts to global electron loss in the radiation belts. *Journal of Geophysical Research: Space Physics*.
- Gurnett, D., Anderson, R., Scarf, F., Fredricks, R., & Smith, E. (1979). Initial results from the isee-1 and-2 plasma wave investigation. *Space Science Reviews*, 23(1), 103–122.
- Horne, R. B., & Thorne, R. M. (2003). Relativistic electron acceleration and precipitation during resonant interactions with whistler-mode chorus. *Geophysical Research Letters*, 30(10). Retrieved from <http://dx.doi.org/10.1029/2003GL016973> (1527) doi: 10.1029/2003GL016973
- Joy, S., Kivelson, M., Walker, R., Khurana, K., Russell, C., & Ogino, T. (2002). Probabilistic models of the jovian magnetopause and bow shock locations. *Journal of Geophysical Research: Space Physics*, 107(A10), SMP–17.
- Li, W., Thorne, R., Angelopoulos, V., Bonnell, J., McFadden, J., Carlson, C., ... Auster, H. (2009). Evaluation of whistler-mode chorus intensification on the nightside during an injection event observed on the THEMIS spacecraft. *Journal of Geophysical Research: Space Physics*, 114(A1).
- Li, W., Thorne, R. M., Angelopoulos, V., Bortnik, J., Cully, C. M., Ni, B., ... Magnes, W. (2009). Global distribution of whistler-mode chorus waves observed on the THEMIS spacecraft. *Geophysical Research Letters*, 36(9). Retrieved from <http://dx.doi.org/10.1029/2009GL037595> (L09104) doi: 10.1029/2009GL037595
- Lorentzen, K. R., Blake, J. B., Inan, U. S., & Bortnik, J. (2001). Observations of relativistic electron microbursts in association with VLF chorus. *Journal of Geophysical Research: Space Physics*, 106(A4), 6017–6027. Retrieved from <http://dx.doi.org/10.1029/2000JA003018> doi: 10.1029/2000JA003018
- Lorentzen, K. R., Looper, M. D., & Blake, J. B. (2001). Relativistic electron microbursts during the GEM storms. *Geophysical Research Letters*, 28(13),

- 2573–2576. Retrieved from <http://dx.doi.org/10.1029/2001GL012926> doi: 10.1029/2001GL012926
- Meredith, N., Horne, R., Summers, D., Thorne, R., Iles, R., Heynderickx, D., & Anderson, R. (2002). Evidence for acceleration of outer zone electrons to relativistic energies by whistler mode chorus. In *Annales geophysicae* (Vol. 20, pp. 967–979).
- Metropolis, N., Rosenbluth, A. W., Rosenbluth, M. N., Teller, A. H., & Teller, E. (1953). Equation of state calculations by fast computing machines. *The journal of chemical physics*, 21(6), 1087–1092.
- Millan, R., & Thorne, R. (2007). Review of radiation belt relativistic electron losses. *Journal of Atmospheric and Solar-Terrestrial Physics*, 69(3), 362–377. Retrieved from <http://www.sciencedirect.com/science/article/pii/S1364682606002768> doi: <http://dx.doi.org/10.1016/j.jastp.2006.06.019>
- Mozer, F. S., Agapitov, O. V., Blake, J. B., & Vasko, I. Y. (2018). Simultaneous observations of lower band chorus emissions at the equator and microburst precipitating electrons in the ionosphere. *Geophysical Research Letters*. Retrieved from <http://dx.doi.org/10.1002/2017GL076120> doi: 10.1002/2017GL076120
- O’Brien, T. P., Blake, J. B., & W., G. J. (2016, May). *Aerocube-6 dosimeter data readme* (Tech. Rep. No. TOR-2016-01155). The Aerospace Corporation.
- O’Brien, T. P., Looper, M. D., & Blake, J. B. (2004). Quantification of relativistic electron microburst losses during the GEM storms. *Geophysical Research Letters*, 31(4). Retrieved from <http://dx.doi.org/10.1029/2003GL018621> (L04802) doi: 10.1029/2003GL018621
- O’Brien, T. P., Lorentzen, K. R., Mann, I. R., Meredith, N. P., Blake, J. B., Fennell, J. F., ... Anderson, R. R. (2003). Energization of relativistic electrons in the presence of ULF power and MeV microbursts: Evidence for dual ULF and VLF acceleration. *Journal of Geophysical Research: Space Physics*, 108(A8). Retrieved from <http://dx.doi.org/10.1029/2002JA009784> doi: 10.1029/2002JA009784
- Olson, W. P., & Pfitzer, K. A. (1982). A dynamic model of the magnetospheric magnetic and electric fields for July 29, 1977. *Journal of Geophysical Research: Space Physics*, 87(A8), 5943–5948. Retrieved from <http://dx.doi.org/10.1029/JA087iA08p05943> doi: 10.1029/JA087iA08p05943
- Parks, G. K. (1967). Spatial characteristics of auroral-zone X-ray microbursts. *Journal of Geophysical Research*, 72(1), 215–226.
- Sambridge, M., Gallagher, K., Jackson, A., & Rickwood, P. (2006). Trans-dimensional inverse problems, model comparison and the evidence. *Geophysical Journal International*, 167(2), 528–542.
- Santolik, O., Gurnett, D., Pickett, J., Parrot, M., & Cornilleau-Wehrlin, N. (2003). Spatio-temporal structure of storm-time chorus. *Journal of Geophysical Research: Space Physics*, 108(A7).
- Shumko, M., Sample, J., Johnson, A., Blake, B., Crew, A., Spence, H., ... Handley, M. (2018). Microburst scale size derived from multiple bounces of a microburst simultaneously observed with the firebird-ii cubesats. *Geophysical Research Letters*, 45(17), 8811–8818. Retrieved from <https://agupubs.onlinelibrary.wiley.com/doi/abs/10.1029/2018GL078925> doi: 10.1029/2018GL078925
- Thorne, R. M., O’Brien, T. P., Shprits, Y. Y., Summers, D., & Horne, R. B. (2005). Timescale for MeV electron microburst loss during geomagnetic storms. *Journal of Geophysical Research: Space Physics*, 110(A9). Retrieved from <http://dx.doi.org/10.1029/2004JA010882> (A09202) doi: 10.1029/2004JA010882
- Van Allen, J. A. (1959). The geomagnetically trapped corpuscular radiation. *Journal of Geophysical Research*, 64(11), 1683–1689. Retrieved from <http://dx.doi.org/10.1029/JZ064i011p01683> doi: 10.1029/JZ064i011p01683

- 516 Vernov, S., & Chudakov, A. (1960). Investigation of radiation in outer space. In *In-*
517 *ternational cosmic ray conference* (Vol. 3, p. 19).
- 518 Woodger, L., Halford, A., Millan, R., McCarthy, M., Smith, D., Bowers, G., ...
519 Liang, X. (2015). A summary of the BARREL campaigns: Technique for
520 studying electron precipitation. *Journal of Geophysical Research: Space*
521 *Physics*, 120(6), 4922–4935.